

Globular to lamellar transition during anomalous eutectic growth

Wei Lei^{1,2,5} , Cao Yongqing³, Lin Xin^{1,2,5}, Chang Kun⁴ and Huang Weidong^{1,2}

¹ State Key Laboratory of Solidification Processing, Northwestern Polytechnical University, 127 Youyixilu, Xi'an, Shaanxi 710072, People's Republic of China

² Key Laboratory of Metal High Performance Additive Manufacturing and Innovative Design, MIIT China, Northwestern Polytechnical University, Xi'an, Shaanxi 710072, People's Republic of China

³ Luoyang Institute of Science and Technology, Luoyang, 471000, People's Republic of China

⁴ Shanghai Aircraft Design and Research Institute, COMAC, Jinke Road 5188, Shanghai 201210, People's Republic of China

E-mail: weilei@nwpu.edu.cn and xlin@nwpu.edu.cn

Received 2 February 2020, revised 8 July 2020

Accepted for publication 14 July 2020

Published 7 August 2020



CrossMark

Abstract

As a typical solidification microstructure, anomalous eutectic is still not known of its growth mechanism. Mullis *et al* (2018, *Acta Mater.* 145:186) experimentally showed that the volume fraction of anomalous eutectic was not consisted with the predictions by any model invoking partial remelting of primary solidified microstructure. In the present article, the anomalous eutectic microstructure of Ni–Sn alloy solidified from undercooled melts and laser remelting melt pool has been investigated through experiments and cellular automaton (CA) simulations. Computational and experimental results showed that the nucleated α -Ni particulates grew into globular, lamellar or ‘tadpole’ morphology. The ‘tadpole’ morphology, which has a globular ‘head’ and a lamellar ‘tail’, is an intermediate pattern between globular and lamellar morphologies, and would be seen as an evidence of the globular to lamellar transition (GLT). The occurrence of the GLT or not determines that the solidified microstructure is either anomalous eutectic or lamellar eutectic. CA simulations showed that the GLT was mainly influenced by the temperature gradient G and pulling velocity V . For positive G and V , representing the directional solidification at the bottom of melt pool, the GLT prefers to occur at high G and low V ; for negative G and V , which refers to the solidification in undercooled melts, the GLT prefers to occur at low absolute value of G and V . The GLT was also experimentally observed under

⁵ Authors to whom any correspondence should be addressed.

the above two circumstances. The GLT growth mechanism abstained from CA simulations well explains the experimental results.

Keywords: solidification, eutectic growth, cellular automaton method, anomalous eutectic

(Some figures may appear in colour only in the online journal)

1. Introduction

Eutectic is one of the most commonly observed solidification microstructure [1]. Steady-state lamellar eutectic grows close to the minimum-undercooling spacing λ_{JH} in the Jackson and Hunt's eutectic theory [2], which is proportional to a function of pulling velocity $V^{-1/2}$ and independent of temperature gradient G . Anomalous eutectic is also an important eutectic microstructure, which is less understood than lamellar eutectic. Experimental investigations on anomalous eutectic solidified from deep undercooled melts have been continued for several decades [3–15]. Recently, the anomalous eutectic has also been observed during laser remelting of Ni–Sn alloy [16–19]. The typical morphologies of anomalous eutectic microstructure has been characterized as its globular pattern [20]. Electron backscatter diffraction pattern (EBSD) analysis of Ni–Sn anomalous eutectic has shown that the α -Ni solid solution was randomly oriented within continuous β -Ni₃Sn intermetallic compound [9]. The EBSD analysis [19] has also shown that the remelting of α -Ni dendrites had positive effects on the nucleation of anomalous α -Ni particulates.

The microstructure evolution of anomalous eutectic growth has been commonly found to be coexist with lamellar eutectic [6]. Thus, the volume fraction of the anomalous eutectic is an important aspect for the characterization of anomalous eutectic growth [13]. For the solidification in deep undercooled melts, the volume fraction of anomalous eutectic increases as the increasing of bulk melt undercooling ΔT [21]. Many anomalous eutectic growth models have been established based on the partial remelting of primary dendrites or eutectic. Li *et al* [10] have made a hypothesis that anomalous eutectic in undercooled Ni–Sn alloys structure was formed by partial remelting of primary solidified structure (Ni-rich or eutectic dendrites) and subsequent recrystallization of the β -Ni₃Sn matrix from the remaining liquid. Wei *et al* [14] have presented a remelting induced anomalous eutectic growth model based on the eutectic dendrite growth theory. Recently, Mullis *et al* [15] have shown that the volume fraction of anomalous eutectic observed far exceeds the volume fraction that would be expected to form during the recalescence stage of solidification.

Due to the rapid solidification in bulk undercooled melts and the fast moving melt pool under laser spot, both of the two solidification processes are difficult for real-time observation. Numerical simulation [22–25] would be an appropriate method for investigating the anomalous eutectic microstructure evolution. In order to establish a numerical model for anomalous eutectic growth, the evolution of temperature field is fundamental. Compared to deep undercooled melts, the temperature field during laser remelting process could be simplified into directional solidification, which have been commonly applied for the simulation of microstructure evolution in melt pool [26–29]. Thus the quantitative simulation of anomalous eutectic growth in the melt pool during laser remelting would be possible. So far as we know, only a few simulations results of the anomalous eutectic growth in the melt pool during laser additive manufacturing were shown [30–32].

Our previous studies [30, 31] have shown that the cooling rate at the bottom of melt pool was a linear function of time t . Cellular automaton (CA) simulations also repro-

duced the anomalous eutectic morphologies at the bottom of melt pool, which agreed well with experimental results. However, the fundamental anomalous eutectic growth mechanism is still not clarified. For instance, why does a particulate grow from globular to lamellar morphology? In the present article, it is focused on the morphological change of one single particulate, which would give details of the morphological evolution during anomalous eutectic growth. The identifications of anomalous eutectic growth morphologies in previous researches were also sketchy, briefly identifying that it was much coarser and globular than lamellar eutectic [15]. In the present study, we subdivide the anomalous morphologies into three types: globular, ‘tadpole’ and coarse lamellar morphologies. The ‘tadpole’ microstructure refers to the globular morphology with a lamellar tail. This particular morphology should be seen as the occurrence of the globular to lamellar transition (GLT). The influence factors on the GLT are the main contributions from the experimental and computational investigations in the present article. With the understanding of the GLT, the anomalous eutectic growth mechanism has been clarified.

2. Experimental procedures

Two experiments have been made to observe the anomalous eutectic morphologies: one was the solidification in deep undercooled melts; the other was laser remelting process. A scanning electron microscope of TESCANVEGAI-LMH was used to observe the microstructure.

2.1. Anomalous eutectic growth from deep undercooled melts

The experiments were according to Guo *et al* [33], however, a Ni-32.5 wt% Sn alloy was used. The Ni–Sn alloy was prepared by arc melting of 99.98% purity Ni ingot and 99.999% purity Sn ingot at a vacuum of 4.0×10^{-3} Pa. The experiment was made in an induction furnace containing 5 g Ni-32.5 wt% Sn alloy under protection of melted B₂O₃ glass. After cyclic overheating and cooling processes, the alloy was cleaned so that a deep undercooling was obtained. The solidified specimen was cut through the largest sectional area.

2.2. Anomalous eutectic growth from melt pool during laser remelting

The experiments were designed by laser remelting twice on the Ni-30 wt% Sn alloy powders under the same process parameters. The laser power was 100 W, and two laser scanning velocities L was used, 1.0 mm s^{-1} and 2.0 mm s^{-1} . Ni-30 wt% Sn alloy powders were produced by a plasma rotating electrode process (PREP) technology. Due to the powders have higher laser absorptivity and lower thermal conductivity, the melt pool formed during the first remelting was larger than that during the second remelting process. The remelted specimens were cut along the transverse direction, which was vertical to the scanning direction of the laser beam. The benefit of laser remelting twice is that the fine lamellar eutectic from the first laser remelting would be the initial microstructure for the second laser remelting. By changing the laser scanning velocity, the correlation between the laser scanning velocity and the volume fraction of anomalous at the bottom of melt pool can be obtained.

3. Numerical simulation model

A cellular automaton (CA) model is used for the numerical simulations of anomalous eutectic in the present article [31]. CA model has been widely used in simulations of grain growth [34], dendritic growth [35] and eutectic growth [36].

The solute diffusion is governed by:

$$\frac{\partial C_l}{\partial t} = D_l \nabla^2 C_l + C_l(1 - k_\alpha) \frac{\partial f_{s,\alpha}}{\partial t} + C_l(1 - k_\beta) \frac{\partial f_{s,\beta}}{\partial t} \quad (1)$$

where C_l is the solute concentration, t is time, D_l is the solute diffusion coefficient, k_α and k_β are the partition coefficients of α and β phases, $f_{s,\alpha}$ and $f_{s,\beta}$ are the solid fractions. The solute diffusion in solid phase is neglected in present CA model. The governing equation is solved by an explicit finite difference method. The left and right boundary conditions are periodic, the bottom boundary is the initial eutectic, and the up boundary is fixed concentration C_0 .

The interfaces kinetics of eutectic growth is related to the local equilibrium condition:

$$T_i^* = T_E + m_{l,i}(C_{l,i}^* - C_E) - \Gamma_i K_i f(\phi_i, \theta_i) \quad (2)$$

where T_i^* is the interface temperature, the subscript $i = \alpha$ or β , T_E is the eutectic temperature, $m_{l,i}$ is the liquidus slope, $C_{l,i}^*$ is the solute concentration at SL interface, C_E is the eutectic concentration, Γ_i is the Gibbs–Thomson coefficient, K_i is the interface curvature, $f(\phi_i, \theta_i) = 1 - 15\varepsilon_i \cos(4(\phi_i - \theta_i))$, representing the interface energy anisotropy, ϕ_i is the angle between the interface normal and the x axis, θ_i is the angle of crystal orientation to the x axis, ε_i is the interface energy anisotropy coefficient.

In the present CA model, the computational domain is divided into uniform rectangular cells. Each cell should be one of the six states: liquid, α interface, β interface, α solid, β solid, and three phases interface states. The α solid state means a cell full of α phase in solid state, and the α interface state is a mixture of α solid and liquid. Consequently, the three phases interface state is a mixture of α solid, β solid and liquid. Thus, the eutectic growth is the combination growth of all of the interface cells. The growth of α or β interface cells follows the single phase growth kinetics, which is the same as that during dendritic growth. The three phases interface cell allows the α and β phases growing independently into the remained liquid phase, until it is full of solid α and β phases. If the α solid fraction is greater than 50%, it is marked as α solid state; otherwise it will be changed into β solid cell. The details of present CA model are seen in our recent paper [31].

The present CA model has several advanced features:

- (a) The addition of a three phases interface state in CA model satisfied the continuous lateral growth of the interphase boundary, which is important for the lamellar eutectic instabilities. Thus, it is the first time for CA model to obtain the transition from period-preserving oscillatory ($1\lambda O$) pattern to period-doubling oscillatory ($2\lambda O$) pattern [31].
- (b) In the present CA model, we used height function method [37] to improve the accuracy of interface curvature calculation, which was implemented for the first time in CA model. The simulation results have shown that the accuracy of curvature calculation was greatly improved [31], which was fundamental for a quantitative CA model.

3.1. Characterization of anomalous eutectic morphology

The anomalous eutectic morphologies were obtained from two solidification processes: one was solidification by laser remelting process, the other was the solidification from undercooled melts, as seen in figures 1(a) and (b). Figure 1(a) is the anomalous eutectic obtained at the bottom of melt pool during laser remelting of Ni–Sn alloy with laser scanning speed 1.0 mm s^{-1} . Figure 1(b) shows the anomalous microstructure solidified from undercooled melts with undercooling of 70 K. In both of the two figures, the dark phase is the α -Ni, and the light

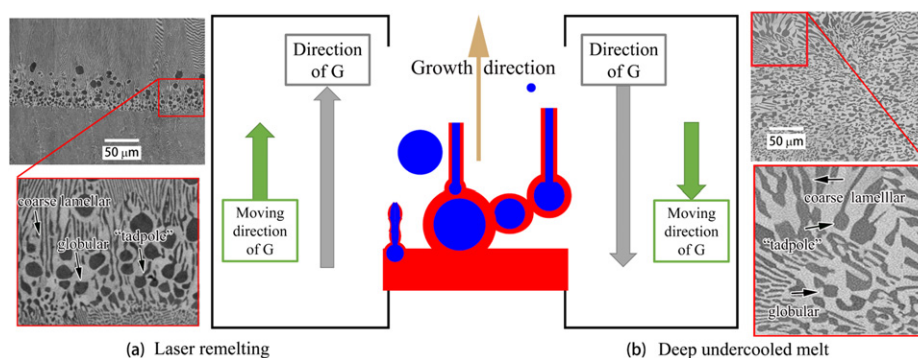


Figure 1. The anomalous eutectic microstructure of Ni–Sn alloy for laser remelting solidification and deep undercooled melts solidification, and they have opposite direction of temperature gradient G and its moving direction: (a) the solidification at the bottom of melt pool under the laser scanning speed 1.0 mm s^{-1} ; (b) solidification from undercooled melts with the undercooling 70 K .

phase is the $\beta - \text{Ni}_3\text{Sn}$. Figure 1 also shows that direction of temperature gradient and its moving direction for the two solidification processes are opposite.

The anomalous eutectic growth has been well investigated by measuring the volume fractions and the theoretical analysis of the correlation between the lamellar spacing and cooling rate [15]. However, the identifications of anomalous eutectic morphology in previous research were sketchy, briefly identifying that it was much coarser and globular than lamellar eutectic. In the present study, the anomalous morphologies were subdivided into three classes: globular, ‘tadpole’ and coarse lamellar morphologies, as seen in figures 1(a) and (b). Among all various anomalous $\alpha\text{-Ni}$ morphologies, the ‘tadpole’ $\alpha\text{-Ni}$ morphology has not been paid much attention. The differences between the globular and ‘tadpole’ morphology are whether there is a lamellar eutectic tail. The ‘tadpole’ $\alpha\text{-Ni}$ particulates morphologically show that they are critical patterns between the globular and lamellar morphologies, and would be seen as an evidence of the GLT. The understanding on the growth mechanism of ‘tadpole’ $\alpha\text{-Ni}$ morphology would help to explain the transition from anomalous eutectic to lamellar eutectic. Based on the understanding of the GLT, a new anomalous eutectic growth mechanism was proposed for the two solidification processes.

3.2. CA simulation of the anomalous eutectic growth

Anomalous eutectic has been observed in both of the solidification from undercooled melts and laser remelting. However, the two processes have opposite thermal conditions, as seen in figure 1. The positive or negative of temperature gradient G and its moving direction (also means its pulling velocity) V are corresponding to the growth direction, as seen in figure 1. Both of the two solidification cases, the growth directions are upward. For deep undercooled melts, the temperature gradient G and its moving direction V are away from the growth direction of anomalous eutectic. For laser remelting solidification, they are along the growth direction of anomalous eutectic. The thermal conditions of laser remelting solidification are straightforward to be simplified into directional solidification, which have been commonly applied for the simulation of the microstructure evolution [26, 27]. So the present CA simulations of directional solidification of Ni–Ni₃Sn anomalous eutectic growth are mainly correlated to laser remelting process. Due to the high energy input and absorption, which result in high temperature

Table 1. Thermal physical parameters of Ni–Ni₃Sn.

Parameters	Ni–Ni ₃ Sn [38]
Eutectic temperature (T_E)	1403 K
Eutectic concentration (C_E)	32.5 wt%
α liquidus slope at T_E (m_α)	–29.7 K/wt%
β liquidus slope at T_E (m_β)	52.4 K/wt%
α partition coefficient (k_α)	0.57
β partition coefficient (k_β)	1.21
Diffusion coefficient of solute (D_i)	$5.0 \times 10^{-9} \text{ m}^2 \text{ s}^{-1}$
α Gibbs–Thomson coefficient (Γ_α)	$2.98 \times 10^{-7} \text{ m K}$
β Gibbs–Thomson coefficient (Γ_β)	$2.1 \times 10^{-7} \text{ m K}$

gradient and high cooling rate, the latent heat of solidification and recalescence phenomenon were neglected.

For deep undercooled melts, negative temperature gradient G and negative pulling velocity V were used. The latent heat of solidification and recalescence phenomenon were also neglected, based on the considering that anomalous eutectic grows after the recalescence phenomenon. The simulation parameters of negative G and V were empirically given, because the thermal conditions of deep undercooled melts were less understood than that of laser remelting process.

The physical parameters were according to references [10, 38], as seen in table 1. The lamellar spacing observed from experiments was quite small, about $0.5 \mu\text{m}$, as seen in figure 1(a). And the curvature calculation in the present CA model needs at least several grids. So we used small mesh size of $0.01 \mu\text{m}$ to give quantitative results. Anomalous eutectic growth of the Ni–Sn alloy has been observed in hypoeutectic [19], eutectic [4], and hypereutectic compositions [39]. After the first remelting process, as seen in figure 1(a), the concentration of lamellar eutectic would locally be close to the eutectic concentration Ni-32.5 wt% Sn. So in CA simulations, Ni-32.5 wt% Sn alloy was used in order to get the fundamental understanding of anomalous eutectic growth.

In the following subsections, the simulations of directional solidification Ni–Sn lamellar eutectic were carried out. We mainly focused on the growth of globular and ‘tadpole’ morphologies in order to obtain the influence factors on the GLT.

3.2.1. CA simulation of the globular and ‘tadpole’ morphologies. In order to investigate the growth of globular and ‘tadpole’ morphologies, eight globular α -Ni particulates were set parallel in front of the initial lamellar eutectic, representing the nucleation or partially remelted particulates, as seen in figure 2(a). The initial lamellar spacing was set to $0.5 \mu\text{m}$. The red phase is Ni₃Sn, and the blue phase is the α -Ni. The radius of the particulates increased from $0.2 \mu\text{m}$ to $1.25 \mu\text{m}$. The temperature gradient G and pulling velocity V were shown in each simulation snapshot.

The numbers of time steps during the simulations in figure 2(a) were set different correspond to the G , in order to have the same temperature. However, for each case the time steps were large enough to observe the occurrence of the GLT, because the GLT occurred within very small time scale, as seen in figure 2(c). So the morphologies of the particulates in figures 2(a) and (b) would not change during the following simulations.

Figure 2(a) shows that under the current $V = 1.0 \text{ mm s}^{-1}$ and $G = 0.5 \times 10^6 \text{ K m}^{-1}$, all the particulates are wrapped by Ni₃Sn phase. The globular morphologies did not grow into ‘tadpole’ patterns, corresponding to the experimental globular morphologies in figure 1(a).

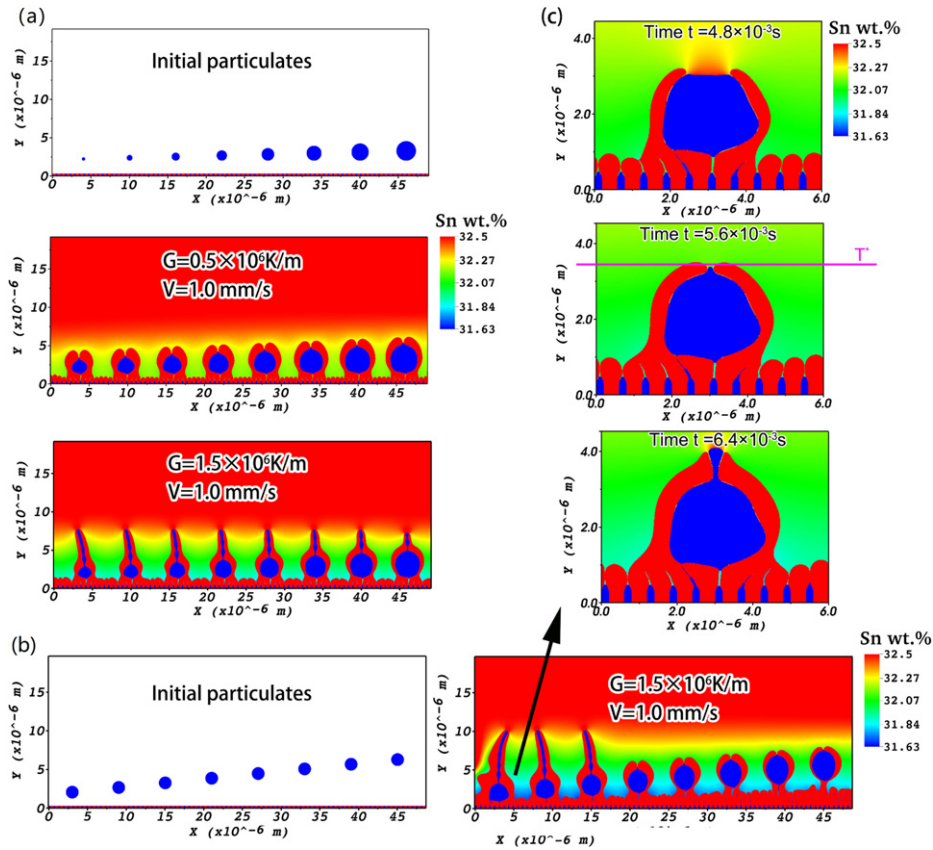


Figure 2. CA simulation of globular α -Ni particulates growing in front of the initial lamellar eutectic: (a) the initial radius of globular particulates gradually increased from $0.2 \mu\text{m}$ to $1.25 \mu\text{m}$ under temperature gradient is $G = 0.5 \times 10^6 \text{ K m}^{-1}$ and the pulling velocity is $V = 1.0 \text{ mm s}^{-1}$; (b) the initial globular particulates had uniform radius of $0.75 \mu\text{m}$ and the vertical position y increased from $2.0 \mu\text{m}$ to $6.3 \mu\text{m}$ under $V = 1.0 \text{ mm s}^{-1}$ and $G = 1.5 \times 10^6 \text{ K m}^{-1}$; (c) simulation of one globular α -Ni particulate from the beginning to the end of the GLT, T^* is defined as the GLT temperature.

Under the same initial condition, when the G increased to $1.5 \times 10^6 \text{ K m}^{-1}$, the ‘tadpole’ morphologies were obtained, which was also shown in figure 2(a). The lamellar tail was generated before the globular α -Ni was totally wrapped.

In figure 2(a), all of the eight particulates are either globular or ‘tadpole’, which were depended on the G . From the present CA simulations, it can be seen that the increasing of the G promotes the GLT to occur. And the GLT is not influenced by the size of the particulates.

Figure 2(b) was also under $V = 1.0 \text{ mm s}^{-1}$ and $G = 1.5 \times 10^6 \text{ K m}^{-1}$, except that the initial globular particulates had uniform radius of $0.75 \mu\text{m}$ and the vertical position y increased from $2.0 \mu\text{m}$ to $6.3 \mu\text{m}$. It can be seen that only the lowest three globular particulates obtained the ‘tadpole’ morphologies, the rest of the particulates remained globular. The present CA simulation indicates that the more a α -Ni particulate close to the Ni_3Sn interface front, the greater probability for the growth of the ‘tadpole’ morphology is. From figures 2(a) and (b), it is shown that the GLT is not influenced much by the particulate size, but it is sensitive to its position. The sensitivity to the particulates’ position mean that the GLT is controlled by the growth undercooling.

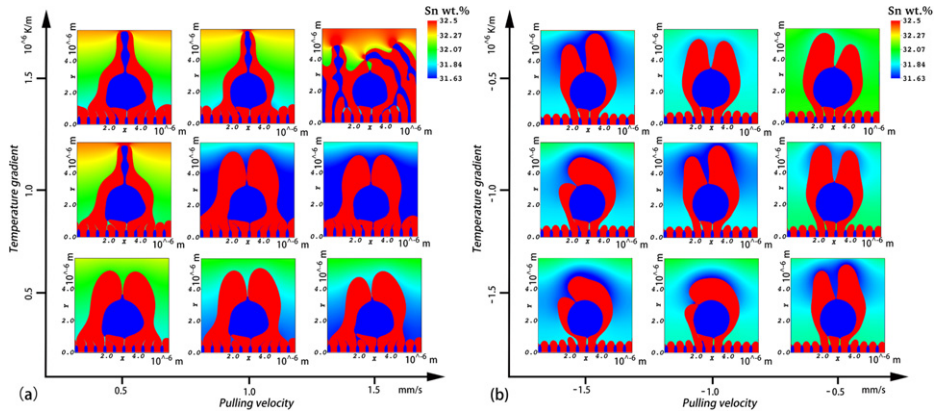


Figure 3. CA simulation of one globular α -Ni particulates growing in front of the initial lamellar eutectic under different G and V showing in the coordinates: (a) positive pulling velocity and temperature gradient; (b) negative pulling velocity and temperature gradient.

Figure 2(c) is the growth details of the first particulate as seen in figure 2(b). It shows that the GLT occurs within a few microseconds. It should be worthy noting that the occurrence of the GLT is instantaneous. Among all of the simulations, none of the particulates grew into the ‘tadpole’ morphology after the β -Ni₃Sn aureole formed. So, the GLT temperature T^* would be an important parameter to describe the differences in the GLT behavior under various G and V .

3.2.2. Effects of V and G on the globular and ‘tadpole’ morphologies. In this section, quantitative results are shown to illustrate the influences of V and G on the globular and ‘tadpole’ morphologies. In section 3.2.1, it has been found that the increasing of the G has positive effects on the GLT, which is not influenced by the particulate radius. In the present simulations, only one α -Ni particulate with fixed radius of $0.75 \mu\text{m}$ and vertical position $y = 2.0 \mu\text{m}$ was initiated for the sake of computational time.

Figure 3(a) is the simulated morphology map for positive G and V . Each simulated morphology refers to specific V and G , which are shown in the coordinates. The first two columns on the left of figure 3(a) show that the increasing of G has positive effects on the GLT, which is the same to section 3.2.1. However, when the $V = 1.5 \text{ mm s}^{-1}$, as seen in the third column of figure 3(a), the GLT is not occurred for all of the three temperature gradients, which indicates that the increasing of V has negative effects on the GLT. Furthermore, under the same cooling rate $R = VG$, different combinations of V and G provide different simulated morphologies, as seen the simulated results by $G = 1.0 \times 10^5 \text{ K m}^{-1}$, $V = 0.5 \text{ mm s}^{-1}$ and $G = 0.5 \times 10^5 \text{ K m}^{-1}$, $V = 1.0 \text{ mm s}^{-1}$. Under higher G and lower V , the ‘tadpole’ morphologies are shown; under lower G and higher V , the globular morphologies are obtained.

The simulations of anomalous eutectic growth in figure 3(a) were mainly for the laser remelting process, where positive G and V were used. The anomalous growth mechanism under negative G and V , which would be seen as the solidification from undercooled melts, has been less considered in the present article. One of the reasons is that the magnitude of the G and V resolved within millimeter in undercooled melts is difficult to be estimated. Even so, the anomalous eutectic growth mechanism under negative G and V should be simulated. For comparison, the growth of globular particulates in figure 3(a) was simulated once more, where the negative G and V were initiated. Figure 3(b) shows the influences of negative G and V on

Table 2. The correlation between the GLT undercooling ΔT_{GLT} and the occurrence of GLT in figures 3(a) and (b).

Figure 3(a)	GLT undercooling	GLT occurred
$V = 0.5 \text{ mm s}^{-1}, G = 0.5 \times 10^6 \text{ K m}^{-1}$	6.1 K	No
$V = 1.0 \text{ mm s}^{-1}, G = 0.5 \times 10^6 \text{ K m}^{-1}$	6.7 K	No
$V = 1.5 \text{ mm s}^{-1}, G = 0.5 \times 10^6 \text{ K m}^{-1}$	7.7 K	No
$V = 0.5 \text{ mm s}^{-1}, G = 1.0 \times 10^6 \text{ K m}^{-1}$	4.4 K	Yes
$V = 1.0 \text{ mm s}^{-1}, G = 1.0 \times 10^6 \text{ K m}^{-1}$	5.6 K	No
$V = 1.5 \text{ mm s}^{-1}, G = 1.0 \times 10^6 \text{ K m}^{-1}$	6.8 K	No
$V = 0.5 \text{ mm s}^{-1}, G = 1.5 \times 10^6 \text{ K m}^{-1}$	4.2 K	Yes
$V = 1.0 \text{ mm s}^{-1}, G = 1.5 \times 10^6 \text{ K m}^{-1}$	5.1 K	Yes
$V = 1.5 \text{ mm s}^{-1}, G = 1.5 \times 10^6 \text{ K m}^{-1}$	5.8 K	No
Figure 3(b)	GLT undercooling	GLT occurred
$V = -1.5 \text{ mm s}^{-1}, G = -1.5 \times 10^6 \text{ K m}^{-1}$	11.8 K	No
$V = -1.0 \text{ mm s}^{-1}, G = -1.5 \times 10^6 \text{ K m}^{-1}$	10.6 K	No
$V = -0.5 \text{ mm s}^{-1}, G = -1.5 \times 10^6 \text{ K m}^{-1}$	10.2 K	No
$V = -1.5 \text{ mm s}^{-1}, G = -1.0 \times 10^6 \text{ K m}^{-1}$	10.1 K	No
$V = -1.0 \text{ mm s}^{-1}, G = -1.0 \times 10^6 \text{ K m}^{-1}$	8.9 K	No
$V = -0.5 \text{ mm s}^{-1}, G = -1.0 \times 10^6 \text{ K m}^{-1}$	8.3 K	No
$V = -1.5 \text{ mm s}^{-1}, G = -0.5 \times 10^6 \text{ K m}^{-1}$	7.4 K	No
$V = -1.0 \text{ mm s}^{-1}, G = -0.5 \times 10^6 \text{ K m}^{-1}$	7.1 K	No
$V = -0.5 \text{ mm s}^{-1}, G = -0.5 \times 10^6 \text{ K m}^{-1}$	6.7 K	No

the globular and ‘tadpole’ morphologies. All of the nine simulated results were globular, and the GLT has not been observed. It is shown that the GLT is much more difficult to occur under negative G and V . The simulation results of figures 3(a) and (b) have well explained the experimental results, as seen in figures 1(a) and (b). Both of the simulation and experiments showed that the laser remelting solidification has much more GLT particulates than the undercooled melts solidification. It is also explained that the laser remelting solidification has less volume fraction of anomalous eutectic than the undercooled melts solidification.

In order to analysis the influence of growth undercooling on the GLT, we defined the GLT undercooling $\Delta T_{\text{GLT}} = T_{\text{E}} - T^*$, where T_{E} is the eutectic temperature and T^* is the temperature when the GLT is about to occur, as seen in figure 2(c). It is worthy to note that the GLT undercooling describes the undercooling when the $\beta\text{-Ni}_3\text{Sn}$ interface front nearly enclose the $\alpha\text{-Ni}$ particulate. According to this meaning, for any $\alpha\text{-Ni}$ particulate, the GLT undercooling is a unique value, no matter the GLT occurs or not. Thus, the GLT undercooling is a parameter showing the relationship between the occurrence of the GLT and its undercooling.

Table 2 shows the GLT undercooling ΔT_{GLT} obtained from the simulation outputs in figures 3(a) and (b). It can be seen that the three simulations showing the ‘tadpole’ morphologies have the lowest ΔT_{GLT} , which indicates that the globular or anomalous eutectic morphologies prefers high ΔT_{GLT} .

The correlation between ΔT_{GLT} and positive G and V is shown in figure 4(a) for laser remelting solidification, and figure 4(b) is the correlation to negative G and V for deep undercooled melts solidification. For laser remelting solidification, the ΔT_{GLT} decreases as the increasing of G and decreasing of V . For deep undercooled melts solidification, the ΔT_{GLT} decreases when both of G and V are close to zero.

Figure 5 shows the simulated GLT under negative G and V : $G = -1.0 \times 10^5 \text{ K m}^{-1}$ and $V = -0.1 \text{ mm s}^{-1}$, as predicted by figure 4(b). It is worthy to note that, for deep undercooled

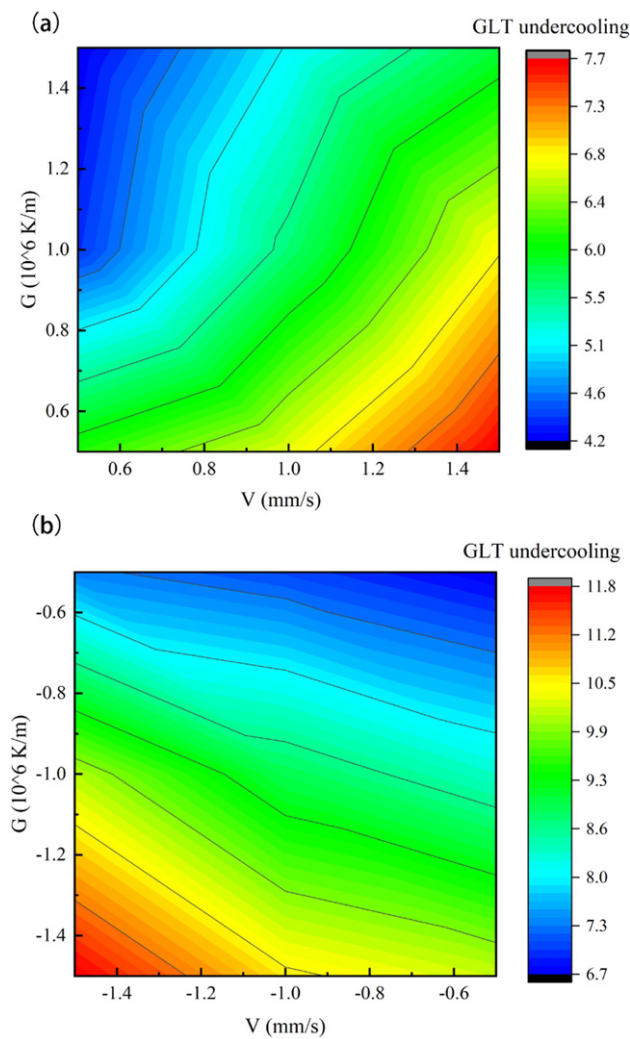


Figure 4. The GLT undercooling as a function of G and V : (a) GLT undercooling data under positive G and V obtained from figure 3(a); (b) GLT undercooling data under negative G and V obtained from figure 3(b).

melts solidification, the lamellar eutectic usually be observed at the end of solidification process, where the absolute values of G and V have been greatly reduced, under which condition the GLT prefers to occur. Present CA simulations agreed with deep undercooled experimental results.

3.2.3. CA simulation of the anomalous eutectic growth with nucleation. CA simulation of the anomalous eutectic growth with nucleation would be a simulation evidence for the GLT mechanism obtained in section of 3.2.1 and 3.2.2. The microstructure evolution in the melt pool during laser remelting or laser metal deposition has been paid much attention [26, 27]. Although the cooling rate R was considered to be varied within the melt pool (commonly distinguished by bottom, middle or top) [26], however, fixed cooling rate R was used for these melt pool positions. Our previous simulation and theoretical analysis [30] showed that the

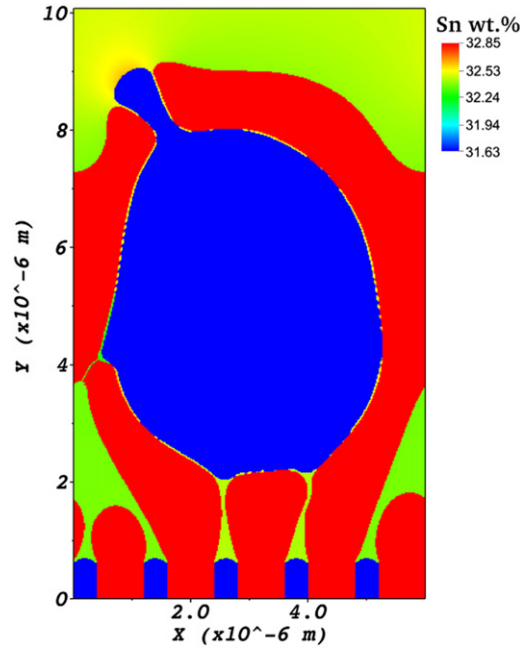


Figure 5. CA simulation of the GLT under negative G and V : $G = -1.0 \times 10^5 \text{ K m}^{-1}$ and $V = -0.1 \text{ mm s}^{-1}$.

cooling rate R at the bottom of melt pool increases as time t increases. So, we used a linearly increasing pulling velocity V under fixed vertical temperature gradient G to approximate the temperature field at the bottom of melt pool [30]. The simulated morphologies agreed well with experimental results. However, in section of 3.2.1 and 3.2.2 of present article, it is discovered that the GLT is individually affected by G and V , which means the cooling rate $R = GV$ is not sufficient to describe the anomalous eutectic growth behavior.

The driving force of the α -Ni nucleation is characterized by the degree of undercooling ΔT considering the thermal and constitutional undercooling effect. The nucleate rate I^{heter} [40] is defined as:

$$I^{\text{heter}} = I_0^{\text{heter}} \exp\left(-\frac{16\pi}{3} \frac{\gamma_{\text{SL}}^3}{(\rho\Delta s_f \Delta T)^2 k_B T} f(\theta)\right) \quad (3)$$

where I_0^{heter} is pre-exponential factor, γ_{SL} is SL interface energy, ρ is density, Δs_f is volume solidification entropy, k_B is Boltzmann's constant, ΔT is undercooling, T is temperature, $f(\theta)$ is the geometric factor of heterogeneous nucleation. For Ni metal, $I_0^{\text{heter}} \approx 10^{22} \text{ m}^{-3} \text{ s}^{-1}$. I^{heter} increases as the ΔT and T increase. Due to the nucleation occurs close to the melt point, the influence of T is ignored in the present simulations. It is worthy to note that equation (3) does not consider the nucleation sites. In the present simulations, a small random perturbation ε was applied to each liquid phase cell. During each step (dt), if the random number ε is smaller than the nucleation probability ($I^{\text{heter}} \times dx^3 \times dt$) of the cell (dx^3), then the nucleation of the α -Ni phase occurs in this cell. The nucleation mechanism in the CA model considers the phenomenon that the nucleation rate increases with ΔT and the fact that the nucleation sites were randomly located.

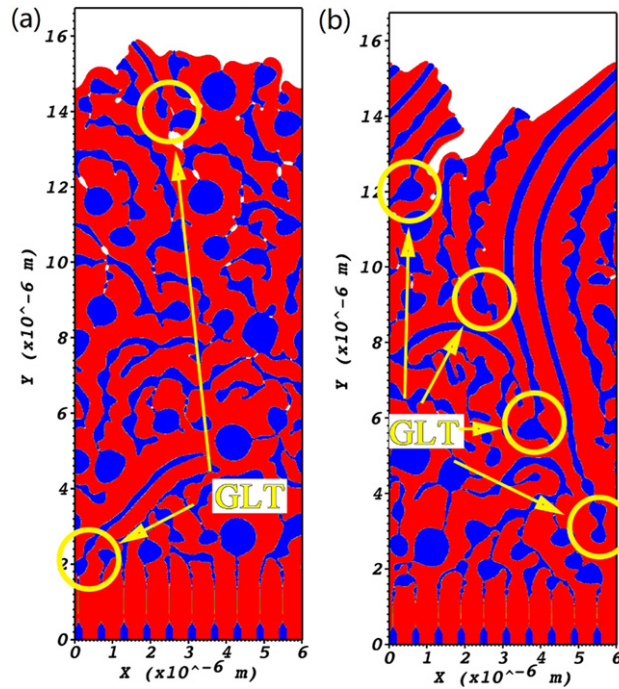


Figure 6. CA simulations of Ni–Sn anomalous eutectic growth under various strategies of vertical pulling velocity V and vertical temperature gradient G : (a) $G = 0.5 \times 10^6 \text{ K m}^{-1}$, $V = 1.0 \text{ mm s}^{-1}$; (b) $G = 1.0 \times 10^6 \text{ K m}^{-1}$, $V = 0.5 \text{ mm s}^{-1}$.

In this section, CA simulations of the anomalous eutectic growth with nucleation under the same cooling rate R with different combinations of G and V are presented, as seen in figure 6. Figure 6(a) was simulated under $G = 0.5 \times 10^6 \text{ K m}^{-1}$ and $V = 1.0 \text{ mm s}^{-1}$, and figure 6(b) was under $G = 1.0 \times 10^6 \text{ K m}^{-1}$ and $V = 0.5 \text{ mm s}^{-1}$. The G and V were selected the same as two snapshots in figure 3(a).

It can be seen that under the same cooling rate, the growth morphologies are quite different: figure 6(a) shows typical globular anomalous eutectic; figure 6(b) shows the lamellar eutectic growth. In figure 6(b), the growth of long lamellar eutectic prevents new nucleation, that is why figure 6(b) has less GLT-s than figure 6(a). It can be seen that above $6 \mu\text{m}$ along Y coordinate, figure 6(b) has much less nucleation than figure 6(a). And it worthy to note that figure 6(b) has larger GLT-s percentage out of nucleation than figure 6(a). So, generally speaking, figure 6(a) has less GLT particulates, and some of them were terminated by other globular particulates. The occurrence of GLT is more obviously observed in figure 6(b), and most of the GLT particulates have been developed into part of lamellar eutectic.

It is worthy to note that high G and low V promote the occurrence of the GLT, which is the same thermal condition at the bottom of melt pool, where the GLT has been experimentally observed, as seen in figure 1(a).

In the present simulations, after nucleation, the α -Ni particulates grew into globular morphologies, instead of dendrites. The reason is that the undercooling ΔT is small. According to the solidification theory, the dendrite tip radius increases as the undercooling ΔT decreases. In the present simulations, the concentration was close to the eutectic concentration C_E and the temperature was also close to the eutectic temperature T_E , both of which indicated that

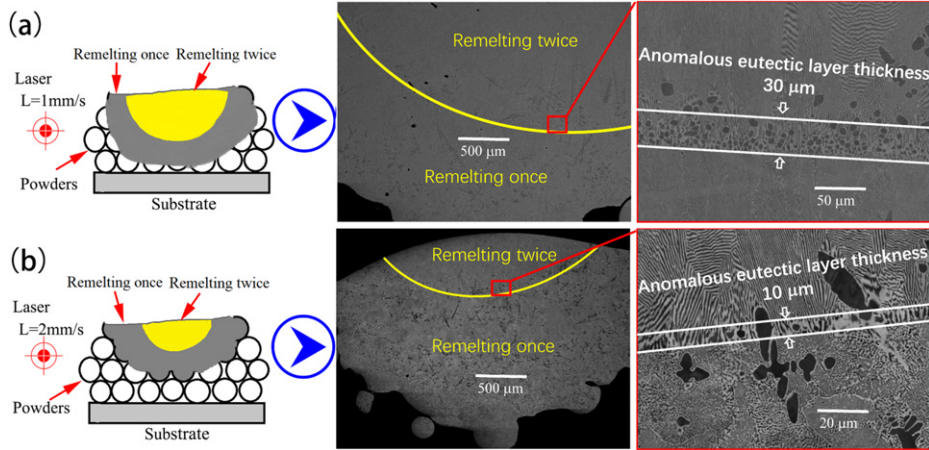


Figure 7. The eutectic microstructure at the bottom of the melt pool after laser remelting twice, the first remelting on the powder bed and the second repeat remelting under the same process parameters: (a) laser scanning speed $L = 1 \text{ mm s}^{-1}$; (b) $L = 2 \text{ mm s}^{-1}$.

the undercooling ΔT was small. However, at the bottom of the melt pool, the large primary dendrites were observed, as seen in figure 7(b). The large primary dendrites were due to the hypoeutectic composition induced primary dendrite growth formed in the first remelting process, which may be partially melted during the second remelting process.

3.3. Experimental results of laser scanning speed on the growth of anomalous eutectic

The anomalous and lamellar eutectic at the bottom of the melt pool after laser remelting twice could be well distinguished, as seen in figure 7. The melt pool shape and the microstructure are shown in figure 7 for laser scanning speed $L = 1.0 \text{ mm s}^{-1}$ and $L = 2.0 \text{ mm s}^{-1}$. The enlarged view shows the anomalous eutectic layer at the bottom of the melt pool after the second laser remelting. The thickness of the anomalous eutectic layer is $30 \mu\text{m}$ when $L = 1.0 \text{ mm s}^{-1}$. When $L = 2.0 \text{ mm s}^{-1}$, the size of melt pool decreases, and the thickness of the anomalous eutectic layer also decreases to $10 \mu\text{m}$.

The thermal simulations of melt pool shapes under various laser scan speeds were carried out by using our previous numerical model [41]. It is shown that the simulated length and depth of the melt pool increased as the laser scanning velocity decreased as seen in figure 8(a), which agrees well with the experiment results in figure 7. Figure 8(b) shows the temperature profile for A1, B1, A2 and B2 lines at the bottom of the two melt pools. Assuming the temperature distribution field reached steady state, thus the temperature profiles of A1, B1, A2 and B2 lines moved with the same speeds L of the laser scanning. The slope of A1 and A2 lines are the vertical temperature gradient G . The cooling rate R at the bottom of melt pool could be calculated from the slope of B1 and B2 temperature profiles, as seen in the equation (4).

$$R = \frac{dT}{dt} = \frac{dT}{\frac{dS}{L}} = \frac{dT \cdot L}{dS} = M_B L \quad (4)$$

where t is time, S is the length of B1 and B2 lines, L is the laser scanning velocity and M_B is the slope of the B1 and B2 lines.

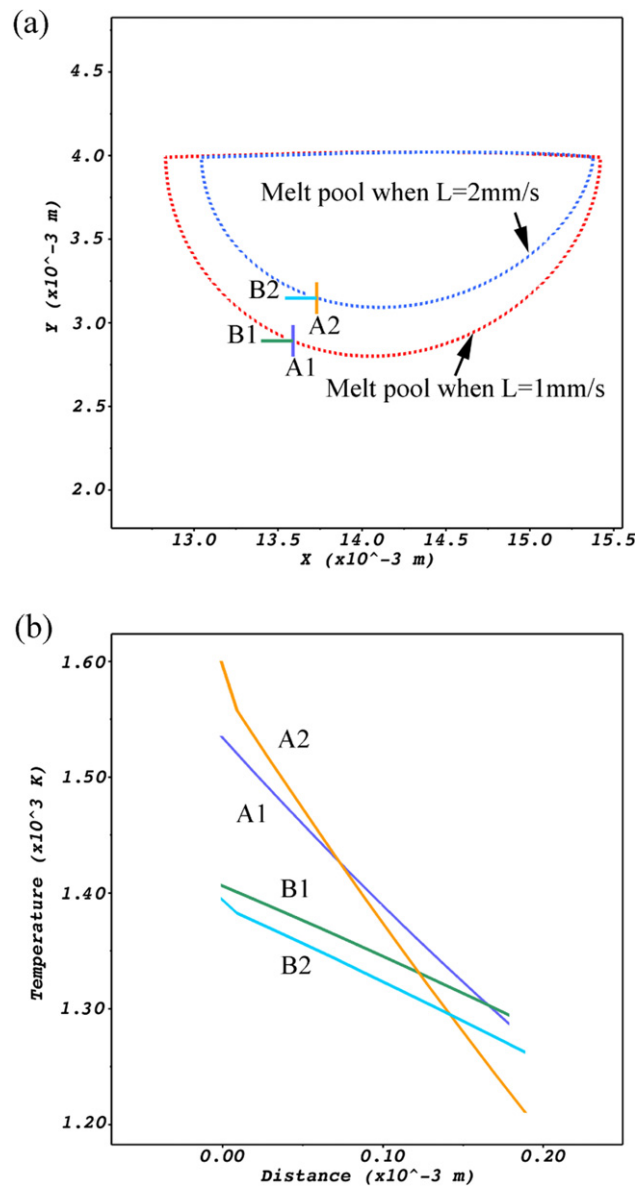


Figure 8. Simulation of the vertical temperature gradient at the bottom of melt pool and the comparison between laser scanning speed of 1.0 mm s^{-1} and 2.0 mm s^{-1} : (a) the melt pool shapes and the locations of A1, B1, A2 and B2 lines; (b) temperature distribution at A1, B1, A2 and B2 lines.

Thus, the vertical pulling velocity V (the moving speed of G along the vertical direction) can be calculated by

$$V = \frac{R}{G} = \frac{M_B L}{G}. \quad (5)$$

The values of G and V calculated from figure 8 are shown in table 3. It can be seen that the G increases as the increasing of L , however, V remains at the same level. From the CA simulations

Table 3. The correlation between the laser scanning velocity L , vertical temperature gradient G and vertical pulling velocity V .

Laser scanning velocity L (mm s ⁻¹)	Vertical temperature gradient G (K m ⁻¹)	Vertical pulling velocity V (mm s ⁻¹)
1.0	1.21×10^6	0.43
2.0	1.94×10^6	0.64

in figure 3, it is concluded that high G and low V promote the GLT. Thus, figure 7(b) has larger G than that in figure 7(a). Therefore, it is not surprised that figure 7(b) has narrower anomalous eutectic layer thickness than figure 7(a).

4. Discussions

In the present experimental and computational investigations, the anomalous eutectic morphologies are summarized into three categories: globular, ‘tadpole’ and coarse lamellar morphologies. The three morphology types, from globular to coarse lamellar, progressively evolve to lamellar eutectic. The ‘tadpole’ morphology, which has a globular head and a lamellar tail, is at the core position for the understanding of the GLT.

From CA simulations, as shown in figures 2 and 3, the GLT mechanism is shown by the following:

- The increasing of the temperature gradient G promotes the GLT to occur, and it is not influenced much by the radius of the globular particulate, as seen in figure 2(a).
- The GLT is sensitive to the position away from the solidifying front (vertical distance). The more close to the solidifying front, the GLT has more chance to occur, shown in figure 2(b).
- The cooling rate R should not be a characteristic quantity for describing the anomalous eutectic growth, because the GLT is individually affected by the temperature gradient G and the pulling velocity V . The GLT occurs at higher G and lower V , as seen in figure 3.

For the case of random nucleation, according the theory of columnar to equiaxed transition (CET), it could be derived that the nucleation distance would be close to the front under high G and low V (all the three conditions promote the GLT to occur), and the nucleation distance would be far from the front under low G and high V (all the three conditions promote the GLT not to occur). The findings of (a)–(c) are consistence to each other for the realistic case.

In order to have a better understanding for the realistic solidification process, we defined the GLT temperature T^* and the GLT undercooling ΔT_{GLT} , thus the overall influences of G , V and the given distance would be shown on the ΔT_{GLT} , which is a key parameter to determine whether the GLT occurs. Through the analysis of the GLT undercooling ΔT_{GLT} , as seen from figures 3–5, it is discovered that the low ΔT_{GLT} prompts the GLT to occur, which is satisfied for both of laser remelting and deep undercooled melts solidification processes. However, for laser remelting, in order to get ΔT_{GLT} low enough, it is required high G and low V . For deep undercooled melts, the absolute value of G and V should be close to zero to obtain low ΔT_{GLT} . In order to verify the GLT mechanism, CA simulations under the same cooling rate R with different combinations of G and V were compared. It is shown that under the same R , higher G and lower V prompted the lamellar eutectic growth, and lower G and higher V induced the anomalous eutectic morphologies, as seen in figure 6. Similar results were observed during laser remelting process that wider anomalous eutectic layer thickness

(30 μm) was shown at lower G (resulted by lower laser scan speed $L = 1 \text{ mm s}^{-1}$), and narrower thickness (10 μm) for larger G (resulted by higher laser scan speed $L = 2 \text{ mm s}^{-1}$) as shown in figure 7.

Previous anomalous eutectic growth models were based on the remelting of lamellar eutectic or primary dendrites. In our previous paper (figure 11 in reference [16]), the schematic of the anomalous eutectic growth was also based on the partial remelting theory, which has been recently shown to be infeasible [15]. Mullis *et al* [15] discussed that the volume fraction of anomalous fraction was around an order of magnitude greater than the calculated recalescence solid fraction. Thus, any model invoking partial remelting of primary solidified microstructure is shown to be infeasible. The anomalous growth mechanism in the present investigations is based on the growth of globular particulates and the occurrence of the GLT. In the present model, as long as the GLT does not occur, the upper limit of the volume fraction of anomalous eutectic would be 100%. And the anomalous eutectic growth in the present model is also at a low undercooling, which agrees with experimental results. So the mechanism of anomalous eutectic growth presented in this article explains the formation of large volume fractions of anomalous eutectic in Mullis's quantitative experimental analysis [15]. And it is also an evidence to Powell and Hogan's proposal [3] that the anomalous eutectic was formed by repeated nucleation after overgrowth by the faster-growing phase.

5. Conclusions

Anomalous eutectic growth of Ni–Sn alloy has been investigated by experimental and computational methods. The morphologies of α -Ni phase in anomalous eutectic are identified by globular, 'tadpole', and coarse lamellar, which morphologically shows the evolution of the GLT. It is discovered that the GLT occurs at low GLT undercooling ΔT_{GLT} . CA simulation results indicate that, for laser remelting solidification, low ΔT_{GLT} is satisfied by high temperature gradient G , low pulling velocity V (the moving velocity of G within 1 mm) and short distance from the globular particulate to the solidifying front. And, for deep undercooled melts, both of the G and V should be close to zero to observe the GLT. Experimental results by laser remelting process show that the volume fraction of anomalous eutectic decreases while increasing the laser scanning speed. The decrement of volume fraction of anomalous eutectic is due to the occurrence of the GLT, because higher temperature gradient is obtained at larger laser scanning speed, which would promote the occurrence of the GLT. The anomalous eutectic mechanism obtained in the present investigations well explains the anomalous eutectic growth for both of laser remelting and deep undercooled melts solidification.

Acknowledgments

This research is supported by the National Key Research and Development Program of China (No. 2016YFB1100105), the National Natural Science Foundation of China (Nos. 51604227, 51323008, 51475380 and 51271213), National Basic Research Program of China (No. 2011CB610402), National High Technology Research and Development Program of China (No. 2013AA031103).

ORCID iDs

Wei Lei  <https://orcid.org/0000-0002-8373-6608>

References

- [1] Akamatsu S and Plapp M 2016 Eutectic and peritectic solidification patterns *Curr. Opin. Solid State Mater. Sci.* **20** 46
- [2] Hunt J and Jackson K 1966 Binary eutectic solidification *Trans. Metall. Soc.* **236** 843
- [3] Powell G and Hogan L 1965 Undercooling in silver–copper eutectic alloys *J. Inst. Met.* **93** 505
- [4] Kattamis TZ and Flemings MC 1970 Structure of undercooled Ni–Sn eutectic *Metall. Mater. Trans.* **1** 1449
- [5] Jones B L 1971 Growth mechanisms in undercooled eutectics *Metall. Trans.* **2** 2950
- [6] Wei B, Herlach D, Feuerbacher B and Sommer F 1993 Dendritic and eutectic solidification of undercooled CoSb alloys *Acta Metall. Mater.* **41** 1801
- [7] Wei B, Herlach D, Sommer F and Kurz W 1993 Rapid solidification of undercooled eutectic and monotectic alloys *Mater. Sci. Eng. A* **173** 355–9
- [8] Wang N, Cao C and Wei B 1999 Solidification behaviour of silver–copper alloys in a drop tube *Adv. Space Res.* **24** 1257–61 gravitational effects in materials and fluid sciences
- [9] Li M, Nagashio K and Kuribayashi K 2002 Reexamination of the solidification behavior of undercooled Ni–Sn eutectic melts *Acta Mater.* **50** 3241
- [10] Li J F, Jie W Q, Zhao S and Zhou Y H 2007 Structural evidence for the transition from coupled to decoupled growth in the solidification of undercooled Ni–Sn eutectic melt *Metall. Mater. Trans. A* **38** 1806
- [11] Han X, Yao W and Wei B 2003 Microstructural evolution of rapidly solidified Co–Mo and Ni–Mo eutectic alloys *J. Mater. Sci. Technol.* **19** 553
- [12] Li J F, Li X L, Liu L and Lu S Y 2008 Mechanism of anomalous eutectic formation in the solidification of undercooled Ni–Sn eutectic alloy *J. Mater. Res.* **23** 2139
- [13] Clopet C, Cochrane R and Mullis A 2013 The origin of anomalous eutectic structures in undercooled AgCu alloy *Acta Mater.* **61** 6894–902
- [14] Wei X, Lin X, Xu W, Huang Q, Ferry M, Li J and Zhou Y 2015 Remelting-induced anomalous eutectic formation during solidification of deeply undercooled eutectic alloy melts *Acta Mater.* **95** 44
- [15] Mullis A M and Clopet C R 2018 On the origin of anomalous eutectic growth from undercooled melts: why re-melting is not a plausible explanation *Acta Mater.* **145** 186
- [16] Cao Y-Q, Lin X, Wang Z-T, Wang L-L, Song M-H, Yang H-O and Huang W-D Three-dimensional reconstruction of anomalous eutectic in laser remelted Ni-30 wt% Sn alloy *Sci. Technol. Adv. Mater.* **16** 065007
- [17] Wang Z, Lin X, Cao Y and Huang W 2013 Microstructure evolution in laser surface remelting of Ni-33 wt% Sn alloy *J. Alloys Compd.* **577** 309–14
- [18] Wang Z, Lin X, Cao Y, Liu F and Huang W 2018 Formation of anomalous eutectic in Ni–Sn alloy by laser cladding *Opt. Laser Technol.* **99** 154–9
- [19] Lin X, Cao Y-Q, Wang Z-T, Cao J, Wang L-L and Huang W-D 2017 Regular eutectic and anomalous eutectic growth behavior in laser remelting of Ni-30 wt% Sn alloys *Acta Mater.* **126** 210
- [20] Li M, Nagashio K, Ishikawa T, Yoda S and Kuribayashi K 2005 Microtexture and macrotexture formation in the containerless solidification of undercooled Ni-18.7At. Sn eutectic melts *Acta Mater.* **53** 731
- [21] Zhao S, Li J, Liu L and Zhou Y 2009 Cellular growth of lamellar eutectics in undercooled AgCu alloy *Mater. Charact.* **60** 519–24
- [22] Karma A and Sarkissian A 1996 Morphological instabilities of lamellar eutectics *Metall. Mater. Trans. A* **27** 635
- [23] QIN R and Rob W E 2003 Computer simulations of the aluminium–silicon anomalous eutectic growth based on multiphase field method *Mater. Trans.* **44** 968
- [24] Andrea P and Mathis P 2008 Stability of lamellar eutectic growth *Acta Mater.* **56** 1348
- [25] Folch R and Plapp M 2005 Quantitative phase-field modeling of two-phase growth *Phys. Rev. E* **72** 011602
- [26] Yin H and Felicelli S D 2010 Dendrite growth simulation during solidification in the lens process *Acta Mater.* **58** 1455
- [27] Fallah V, Amooezaei M, Provatas N, Corbin S F and Khajepour A 2012 Phase-field simulation of solidification morphology in laser powder deposition of Ti–Nb alloys *Acta Mater.* **60** 1633
- [28] Keller T et al 2017 Application of finite element, phase-field, and calphad-based methods to additive manufacturing of Ni-based superalloys *Acta Mater.* **139** 244–53

- [29] Acharya R, Sharon J A and Staroselsky A 2017 Prediction of microstructure in laser powder bed fusion process *Acta Mater.* **124** 360–71
- [30] Wei L, Cao Y, Lin X and Huang W Cellular automaton simulation of the growth of anomalous eutectic during laser remelting process *Materials* **11** 1844
- [31] Wei L, Cao Y, Lin X, Wang M and Huang W 2019 Quantitative cellular automaton model and simulations of dendritic and anomalous eutectic growth *Comput. Mater. Sci.* **156** 157–66
- [32] Gránásy L, Tóth G I, Warren J A, Podmaniczky F, Tegze G, Rátkai L and Pusztai T 2019 Phase-field modeling of crystal nucleation in undercooled liquids a review *Prog. Mater. Sci.* **106** 100569
- [33] Guo X, Lin X, Wang Z, Cao Y, Peng D and Huang W 2013 Formation mechanism of anomalous eutectic and microstructure evolution in highly undercooled solidification of Ni-30% Sn alloy *Acta Metall. Sin.* **49** 475–82
- [34] Rappaz M and Gandin C 1993 Probabilistic modeling of microstructure formation in solidification processes *Acta Metall. Mater.* **41** 345–60
- [35] Zhu M F and Stefanescu D M 2007 Virtual front tracking model for the quantitative modeling of dendritic growth in solidification of alloys *Acta Mater.* **55** 1741–55
- [36] Zhu M F and Hong C P 2002 Modeling of microstructure evolution in regular eutectic growth *Phys. Rev. B* **66** 155428
- [37] Cummins S J, Francois M M and Kothe D B 2005 Estimating curvature from volume fractions *Comput. Struct.* **83** 425
- [38] Wu Y, Piccone T J, Shiohara Y and Flemings M C 1987 Dendritic growth of undercooled nickel–tin: part II *Metall. Mater. Trans. A* **18** 925
- [39] Wang Z, Lin X, Cao Y and Huang W 2013 Microstructure evolution in laser surface remelting of Ni 33 wt.% Sn alloy *J. Alloys Compd.* **577** 309
- [40] Dantzig J A and Rappaz M 2009 *Solidification* (Lausanne: EPFL Press)
- [41] Wei L, Lin X, Wang M and Huang W-D Cellular automaton simulation of the molten pool of laser solid forming process *Acta Phys. Sin.* **64** 018103